#### **ORIGINAL PAPER**



# A hybrid model of intercellular tension and cell-matrix mechanical interactions in a multicellular geometry

Lewis E. Scott¹ · Lauren A. Griggs¹ · Vani Narayanan¹ · Daniel E. Conway¹ · Christopher A. Lemmon¹ · Seth H. Weinberg¹,2,3 □

Received: 20 September 2019 / Accepted: 13 March 2020 / Published online: 20 March 2020 © Springer-Verlag GmbH Germany, part of Springer Nature 2020

#### **Abstract**

Epithelial cells form continuous sheets of cells that exist in tensional homeostasis. Homeostasis is maintained through cell-to-cell junctions that distribute tension and balance forces between cells and their underlying matrix. Disruption of tensional homeostasis can lead to epithelial—mesenchymal transition (EMT), a transdifferentiation process in which epithelial cells adopt a mesenchymal phenotype, losing cell—cell adhesion and enhancing cellular motility. This process is critical during embryogenesis and wound healing, but is also dysregulated in many disease states. To further understand the role of intercellular tension in spatial patterning of epithelial cell monolayers, we developed a multicellular computational model of cell—cell and cell—substrate forces. This work builds on a hybrid cellular Potts model (CPM)—finite element model to evaluate cell—matrix mechanical feedback of an adherent multicellular cluster. Cellular movement is governed by thermodynamic constraints from cell volume, cell—cell and cell—matrix contacts, and durotaxis, which arises from cell-generated traction forces on a finite element substrate. Junction forces at cell—cell contacts balance these traction forces, thereby producing a mechanically stable epithelial monolayer. Simulations were compared to in vitro experiments using fluorescence-based junction force sensors in clusters of cells undergoing EMT. Results indicate that the multicellular CPM model can reproduce many aspects of EMT, including epithelial monolayer formation dynamics, changes in cell geometry, and spatial patterning of cell—cell forces in an epithelial tissue.

 $\textbf{Keywords} \ \ Cellular \ Potts \ model \cdot Traction \ forces \cdot Cell \ mechanics \cdot Spatial \ patterning \cdot Epithelial-mesenchymal \ transition \cdot Cell-cell \ junction \ forces$ 

**Electronic supplementary material** The online version of this article (https://doi.org/10.1007/s10237-020-01321-8) contains supplementary material, which is available to authorized users.

- ⊠ Seth H. Weinberg weinberg.147@osu.edu Christopher A. Lemmon clemmon@vcu.edu
- Department of Biomedical Engineering, Virginia Commonwealth University, Richmond, VA, USA
- Department of Biomedical Engineering, The Ohio State University, Columbus, OH, USA
- Davis Heart and Lung Research Institute, The Ohio State University Wexner Medical Center, Columbus, OH, USA

#### 1 Introduction

The epithelium is characterized by polarized sheets of cells that form by self-organization and reside in a mechanical equilibrium (reviewed in Fristrom 1988). This mechanical equilibrium is maintained by regulation of both adhesion between neighboring epithelial cells (cell–cell) and adhesion between epithelial cells and the underlying extracellular matrix (cell–matrix). Cells generate cytoskeletal tension via actomyosin contractility, which is transmitted to the underlying matrix (Weinberg et al. 2017), while cell–cell junctions mechanically couple abutted cells and distribute cytoskeletal tension to neighboring cells. This physical cellular interconnectivity and balance of tension at the cell–matrix and cell–cell interfaces produce a coupled monolayer that acts as a cohesive structure in static equilibrium.

Maintenance of static equilibrium in the epithelial sheet is essential to maintaining barrier and signaling functions of



the epithelial sheet; however, disruption of the static equilibrium plays an important role in both physiological phenomena such as embryogenesis and pathological states including fibrosis and tumorigenesis (Ingber 2005; Ettensohn 1985). Mechanical equilibrium relies on tissue-scale coordination of mechanical dynamics extending beyond local cell-cell and cell-matrix adhesions (Nelson et al. 2005). Local perturbations to the equilibrium state result in localized tension in the monolayer and a disruption to the equilibrium. For example, the cellular phenomenon known as epithelial-mesenchymal transition (EMT), which is essential for embryogenesis and tissue morphogenesis but has also been implicated in tumorigenesis and fibrotic diseases, is initialized by perturbations in cell-cell junctions. This process results in a phenotypic switch in which epithelial cells transdifferentiate into mesenchymal cells (reviewed in Thiery and Sleeman 2006). The perturbation in cell–cell junctions redistributes tension in the monolayer, and cell-matrix adhesion compensates for the resulting localized stress (Scott et al. 2019). As such, spatial patterning of mechanical stress can facilitate phenotypic regulation and is crucial to both maintenance and disruption of tissue homeostasis (Nelson et al. 2005; Ingber 2005; Maruthamuthu et al. 2011; Narayanan et al. 2020).

Previous studies have explored the role of cell-cell junctions in maintaining tensional homeostasis in either epithelial or endothelial monolayers: Increasing cellular contractility has been shown to stimulate formation of cell-cell junctions (Liu et al. 2010), and subsequent transfer of force to the cell-cell junction allows for stress distribution about the monolayer to maintain tensional homeostasis (Nelson et al. 2005; Maruthamuthu et al. 2011). As a result, mechanical gradients form that define spatial patterns and provide positional information within the monolayer. Both in vitro and in silico studies have demonstrated that the forces of a monolayer correspond to its geometry (Li et al. 2018; Mertz et al. 2012).

In this work, we explore the role of cellular adhesion in maintaining tensional homeostasis of epithelial monolayers. To simulate epithelial monolayers, we extended a model recently developed by van Oers, Rens, and colleagues, which consists of a hybrid cellular Potts model (CPM) and finite element model (FEM) (van Oers et al. 2014). The model simulates individual cell traction forces based on their geometric size and shape, as has previously been modeled and validated by one of the senior authors of this work (Lemmon and Romer 2010): Cellular traction forces are proportional to the first moment of area (FMA) about each point in the individual cell geometry. This results in a pattern of traction forces directed toward the cell centroid and proportional to their distance from the cell centroid. These traction forces generate substrate strains which, in addition to cell-cell and cell-matrix interactions, impose thermodynamic constraints and govern the dynamics of individual cells in the CPM. In the current work, we incorporate the formation of cell-cell junctions between neighboring cells to accurately represent the biology of epithelial cells. We extend the Lemmon and Romer FMA model to multicellular clusters and model traction forces based on the multicellular geometry rather than the individual cell. Thus, individual cell traction forces are directed toward and proportional in magnitude to the distance from the centroid of the multicellular cluster, instead of the centroid of the individual cell.

In the original Lemmon and Romer model, each cell is in static equilibrium: Because traction forces are proportional to the first moment of area, and the centroid by definition is the point where the integral of the first moment of area is zero, all traction forces within a cell must sum to zero. However, when we calculate traction forces based on the multicellular cluster, each individual cell is no longer in static equilibrium. Previous studies have suggested that cells in epithelial monolayers exist in a quasi-equilibrium, even when cell-cell junction forces are present (Liu et al. 2010). As such, we model the force applied to the cell-cell junction as the balancing force that opposes the traction forces for that cell, resulting in a quasi-equilibrium for each cell. This assumption has been observed experimentally in epithelial cell pairs, in which the junction force is equal and opposite to the net traction force (Liu et al. 2010), and illustrated based on force balancing principles in small epithelial clusters (Ng et al. 2014). We thus are able to predict the formation of an epithelial monolayer, including epithelial cell geometry, cell-matrix traction forces, and cell-cell junction forces, based on first principles of cell contractility, cell geometry, and thermodynamic energy minimization. Results are compared to in vitro experiments in which epithelial monolayers were grown in a predetermined geometry established by microcontact-printed islands. Cell geometry and cell-cell junction forces are quantified and compared to simulations. To further probe the role of junction forces in tissue homeostasis, we induce phenotypic changes in epithelial clusters via addition of transforming growth factor- $\beta$ 1 (TGF- $\beta$ 1), a known inducer of EMT. To replicate these effects in the model, we change the relative weight of cell-cell and cell-matrix interfacial energies in the CPM and predict how changing phenotype can facilitate disruption of mechanics and morphology in the epithelial sheet.

Simulations demonstrate that traction forces of multicellular colonies scale linearly with the size of the colony, independent of the individual cell geometry. Additionally, we present a minimal analytical model that generalizes to predict the distribution of junction forces across a monolayer: Junction forces are predicted by a quadratic function that is highest at the monolayer center and decays toward the cluster edge. These predictions are independent of individual-cell geometry and are consistent with the existing literature (Trepat et al. 2009).



#### 2 Materials and methods

In this study, we perform in silico and in vitro experiments to investigate intercellular tension and cell-matrix mechanical interactions in a multicellular geometry. Simulations were performed using a lattice-based cell model, the cellular Potts model (CPM), generalized from the Potts model, to simulate epithelial monolayer dynamics (Graner and Glazier 1992). The cell-occupied lattice is superimposed on a finite element lattice to determine substrate strains from simulated traction forces. We build on a prior iteration of the CPM framework recently presented by van Oers et al. (2014). In particular, we extend the first moment of area (FMA) prediction of single cell traction forces to predict the traction forces of a multicellular cluster. Additionally, we predict cell-cell junction forces maintain mechanical homeostasis by requiring that (1) cells in contact are mechanically coupled through cell-cell junctions, (2) the forces at these junctions balance net traction forces for each cell, and (3) the junction force is equal and opposite across a cell-cell adhesion. We compare model predictions of spatial patterning and junction forces with in vitro experiments of TGF-β1-treated epithelial cell monolayers.

#### 2.1 Cellular Potts model

The two-dimensional domain of the CPM lattice  $\Omega$  contains interconnected sites or nodes  $\vec{x} \in \Omega$  with states  $\sigma(\vec{x})$  that denote the indices of distinct "cells." Each distinct cell-occupied site is defined by  $\sigma(\vec{x}) \in \{1,2,3,\ldots\}$ , and an unoccupied site, representing the underlying extracellular matrix, is defined by  $\sigma(\vec{x}) = 0$ . The CPM approximates the effective energy for a given tissue configuration with the Hamiltonian, a sum of terms where each contribution reflects thermodynamic constraints due to different properties of biological cells and together summarizes the configuration energy of the tissue. Here, the Hamiltonian is given by the sum of three terms.

$$H = H_{\text{area}} + H_{\text{contact}} + H_{\text{durotaxis}}.$$
 (1)

The area term  $H_{\rm area}$  approximates the cell area constraint as a deviation of the cell area, relative to a specified target or "ideal" area, such that

$$H_{\text{area}} = \sum_{\sigma} \lambda_{\text{area}} \left( \frac{a(\sigma(\vec{x})) - A_0}{A_0} \right)^2, \tag{2}$$

where  $a(\sigma(\vec{x}))$  is the area of a given cell determined by number of lattice sites occupied by that cell,  $A_0 = 312.50 \, \mu \text{m}^2$  is the target area for all cells, and  $\lambda_{\text{area}} = 500$  is an elasticity coefficient that maps deviations from the target area to a magnitude of energy.

The contact term  $H_{\rm contact}$  represents costs due to contact between neighboring pixels, with different thermodynamic constraints associated with cell-cell and cell-matrix interfaces:

$$H_{\text{contact}} = \sum_{(\vec{x}, \vec{x}')} J(\sigma(\vec{x}), \sigma(\vec{x}')) (1 - \delta(\sigma(\vec{x}), \sigma(\vec{x}')), \tag{3}$$

where  $J(\sigma(\vec{x}), \sigma(\vec{x}'))$  defines the interaction energy between adjacent lattice sites (x, x') and  $\delta(\sigma(\vec{x}), \sigma(\vec{x}'))$  is the Kronecker delta function defined as 1 if  $\sigma(\vec{x}) = \sigma(\vec{x}')$  and 0 otherwise. The cell–cell interface energy  $J(\sigma(\vec{x}), \sigma(\vec{x}'))$  is given by  $J_{\rm cc}$ , and the cell–matrix interface energy  $J(\sigma(\vec{x}), 0)$  is given by  $J_{\rm cm}$ .

Lastly, the durotaxis term  $H_{\rm durotaxis}$  introduced in van Oers et al. (2014) mimics the tendency for cell migration along gradients of mechanical strain. In particular, this term captures preferential cellular extension into lattice sites of higher strain,

$$H_{\text{durotaxis}} = -g(\vec{x}, \vec{x}') \lambda_{\text{durotaxis}} (h(E(\varepsilon_1))(\vec{v}_1 \cdot \vec{v}_m)^2 + h(E(\varepsilon_2))(\vec{v}_2 \cdot \vec{v}_m)^2). \tag{4}$$

The  $\lambda_{\text{durotaxis}} = 1$  term determines cell sensitivity to durotaxis;  $g(\vec{x}, \vec{x}') = 1$  if a cell extends into a target site  $\vec{x}'$  and  $g(\vec{x}, \vec{x}') = -1$  if a cell retracts; and  $\vec{v}_{1/2} \cdot \vec{v}_m$  are defined such that extension and retraction are greatest parallel to the major and minor principal strain axes,  $\vec{v}_1$  and  $\vec{v}_2$ , respectively, and negligible perpendicular to it. Vector  $\vec{v}_m$  defines the direction of the copy attempt,  $\vec{v}_m = \vec{x} - \vec{x}'$ . The sigmoid function h(E) captures the preference for stiffer substrates,

$$h(E(\varepsilon)) = \frac{\alpha}{1 + \exp(-\beta(E(\varepsilon) - E_{\theta}))},$$
 (5)

which assumes this preference has a minimal stiffness for spreading and reaches a maximum  $\alpha = 10$  at rate  $\beta = 5 \times 10^{-4} \, \mathrm{kPa^{-1}}$  and the half-max stiffness as  $E_{\theta} = 15 \, \mathrm{kPa}$ .  $E(\varepsilon)$  is the cell perception of substrate strain stiffening,

$$E(\varepsilon) = E_0 \left( 1 + (\varepsilon/\varepsilon_{st}) H(\varepsilon) \right), \tag{6}$$

where  $\varepsilon_{st} = 0.1$  determines the rate of strain stiffening,  $\varepsilon$  is the substrate strain, and  $E_0 = 10$  kPa is the Young's modulus of the substrate.  $H(\varepsilon)$  is the Heaviside or indicator function, defined such that  $H(\varepsilon) = 1$  for  $\varepsilon \ge 0$  and 0 otherwise. The strain stiffening only affects cell perception of strain stiffening, not the stiffening of the finite element mesh itself (discussed below).

#### 2.2 Finite element analysis

To describe the substrate strain that governs durotaxis, we assume that a uniform, isotropic, and linearly elastic



two-dimensional substrate deforms to cellular traction forces projected from the CPM (described below). The CPM lattice is mapped to the finite element model by relating each CPM lattice element to a finite element node. We solve the linear system

$$\underline{Ku} = \underline{f},\tag{7}$$

for the displacement u at each node, where K is the global stiffness matrix assembled from the stiffness matrix of each element and f is the applied traction forces. Boundary conditions are imposed with the constraint u=0, i.e., the substrate is fixed at the CPM lattice boundary. In maintaining constant material properties during deformation, the element stiffness matrices K are given by

$$\underline{\underline{K}}_{e} = \int_{\Omega_{e}} \underline{\underline{B}}^{T} \underline{\underline{DB}} \, \mathrm{d}\Omega_{e}, \tag{8}$$

where B is the conventional strain-displacement matrix and D is the material property matrix under plane stress conditions.

$$\underline{\underline{D}} = \frac{E_0}{1 - v^2} \begin{bmatrix} 1 & v & 0 \\ v & 1 & 0 \\ 0 & 0 & \frac{1}{2}(1 - v) \end{bmatrix},\tag{9}$$

relating the Young's modulus,  $E_0=10~\mathrm{kPa}$ , and Poisson's ratio,  $\nu=0.45$ , assuming planar stress and using realistic values for substrate material properties (Boudou et al. 2006). Lastly, B relates the local node displacements to the local strains by,

$$\underline{\varepsilon} = \underline{Bu}_n,\tag{10}$$

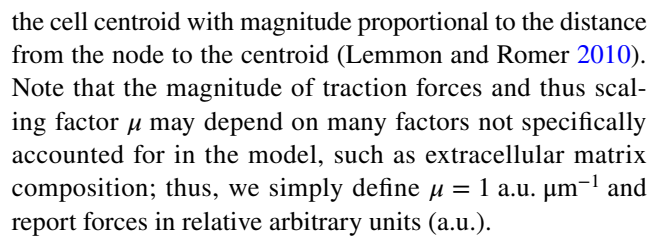
in which  $\underline{\varepsilon}$  is a vector of the strain tensor  $\underline{\varepsilon}$ .

#### 2.3 Traction forces

Prior work of van Oers et al. (2014) assumes that individual cell geometry relates to traction forces in the CPM by the first moment of area (FMA). Application of the FMA model to single cell geometries is previously described by one of the senior authors of this work (Lemmon and Romer 2010). In brief, the single cell FMA model assumes that each site or node i in a CPM cell  $\sigma$  exerts a force on all other nodes j in the same cell that is proportional to the distance between those nodes  $\vec{d}_{i,j}$ ,

$$\vec{F}_i = \mu \sum_j \vec{d}_{i,j},\tag{11}$$

where  $\mu$  is a scaling factor that relates cell geometry to traction forces. Lemmon and Romer previously showed that the resulting traction force at each CPM node is directed toward



Recent experimental evidence demonstrates that traction forces in multicellular clusters are largest at the cluster periphery (Mertz et al. 2012) and further that traction forces scale with cluster size (Mertz et al. 2012; Bazellières et al. 2015), consistent with an extension of the FMA model to multicellular geometries. Here, we extend these previous works of the single cell FMA model to describe the magnitude and direction of traction forces acting about a point in a multicellular geometry and incorporate this model in the CPM framework. For the multicellular FMA model, we assume that the boundary of two cells constitutes a cell-cell junction such that two or more adjacent cells behave as a single structural unit or cluster in mechanical equilibrium. We define an adjacency matrix A, where A is a  $N_{\text{cell}} \times N_{\text{cell}}$  matrix, such that  $A_{\sigma,\sigma'} = 1$  if cells  $\sigma$  and  $\sigma'$  are in contact, and 0 otherwise. By definition, A is symmetric. A cluster is defined as the connected components of the undirected graph defined by A.

Thus, the multicellular FMA model defines the traction force at each node in each CPM cell as directed toward the centroid of the associated multicellular cluster, with magnitude proportional to the distance from the node to the cluster centroid. For the case of a cluster comprised of a single cell, i.e., a cell lacking cell–cell junctions, the multicellular FMA and single cell FMA models are equivalent.

#### 2.4 Intercellular tension

By construction, the single cell FMA model dictates that the sum of traction forces of an individual cell, i.e., the net traction forces  $\vec{T}_{\sigma} = \sum_{i \in \sigma} \vec{F}_i$  for cell  $\sigma$ , is equal to 0. In contrast, using the multicellular FMA model, the net traction forces of an individual cell  $T_{\sigma}$  within a cluster may not be equal to 0. Based on force balancing principles, Ng and colleagues recently predicted that cell–cell junction forces act as a reaction force, balancing the net traction force to maintain static equilibrium of each cell in a multicellular cluster (Ng et al. 2014). Here, we incorporate this concept into the CPM framework using the multicellular FMA: The multicellular FMA model is applied to calculate  $T_{\sigma}$  for each cell, and then we impose mechanical equilibrium on the multicellular clusters by relating the traction force to force across the cell–cell junction, such that for all cells  $\sigma$ ,



$$\sum_{\sigma' \in n_{\sigma}} \vec{J}_{\sigma,\sigma'} + \vec{T}_{\sigma} = 0, \text{ for } \sigma \in (1, \dots, N_{\text{cell}}), \tag{12}$$

where  $n_{\sigma}$  defines the set of "neighbors" of cell  $\sigma$ , i.e.,  $A_{\sigma,\sigma'}=1$ , and  $J_{\sigma,\sigma'}$  is the junction force from cell  $\sigma'$  to cell  $\sigma$ . Equation 12 defines  $N_{\rm cell}$  linear equations, with  $N_{\rm cell}^2$  unknown  $J_{\sigma,\sigma'}$  terms. We further constrain the junction force calculations by assuming that junction force pairs are equal in magnitude and opposite in direction, i.e.,

$$\vec{J}_{\sigma,\sigma'} + \vec{J}_{\sigma',\sigma} = 0,\tag{13}$$

for all  $(\sigma, \sigma')$  such that  $A(\sigma, \sigma') = 1$ . An illustration of the resulting system for a four cell cluster is shown in Fig S1.

Combining Eqs. 12 and 13, we arrive at a linear system with a set of  $N_{\rm cell} + N_{\rm junc}$  equations and  $N_{\rm cell}^2$  unknowns, where  $N_{\rm junc}$  is the number of intercellular junctions, which can be determined by the sum of the terms above (or below) the main diagonal of A, with a maximum value of  $N_{\rm cell}(N_{\rm cell}-1)/2$ . In practice, linear systems for Eqs. 12 and 13 are determined separately to both the x- and y-components of the traction and junction forces.

For nearly all cluster arrangements, the resulting linear system is overdetermined. Analogous to the CPM thermodynamic energy minimization, we assume that the solution to be the minimization of junction force for each cell pair in the cluster, such that  $J_{\sigma,\sigma'}$  terms are calculated as the minimum norm least-squares solution to the linear system (using the MATLAB Isqminnorm function).

### 2.5 Cell division

We incorporate cell division into the CPM model to reproduce epithelial cell capacity to proliferate and form a confluent monolayer. A minimum cell size is necessary for cell proliferation, such that if an individual cell area exceeds a minimum area threshold, given by  $\frac{2}{3}A_0$ , then individual cells divide with random probability  $p_{divide}=0.005$  (unless otherwise stated). For cell division, following the prior approach of Daub and Merks, we compute the line of division for each CPM cell as the line following the minor axis, such that each daughter cell is of approximately equal area (Daub and Merks 2013).

## 2.6 Numerical simulations

Key details of numerical integration, specifically initialization and the iteration for each Monte Carlo step (MCS), are described as follows. The CPM is initialized on a map of pixels, with size  $100 \times 100$ , for which each pixel side corresponds to a size of  $\Delta x = 2.5 \,\mu\text{m}$ . Initial seeding is dispersed on the cell map with random probability,  $p = \Delta x/(4A_0)$ , excluding the outermost boundary. An unloaded finite

element mesh of size  $101 \times 101$  forms the nodes of attachment for cells of the CPM map, in which each cell-occupied pixel is bounded by four nodes.

Iteration of the model describes successive cell movements for each MCS. Cell movement consists of copy attempts of randomly selected pixel. For each pixel to have equal probability of selection, each MCS has a total of 10<sup>4</sup> copy attempts. For each copy attempt, a pixel is selected and randomly perturbed; the sum of interaction energies with each pixel in the Moore neighborhood,  $\sum J(\sigma(x, x'))$ , determines the  $H_{\text{contact}}$  term. Changes in substrate strain govern the  $H_{\text{durotaxis}}$  term. To calculate forces from the CPM, pixels are first mapped to the finite element substrate by identifying the corresponding nodes. At a given instant, the single cell or multicellular geometry is sufficient to define cellular traction forces at each node, using the single cell or multicellular FMA models, as described above, respectively. The resulting traction forces govern the displacement at each node and determines the strain in the finite element mesh, which in turn is used in evaluating  $H_{\rm durotaxis}$ . Lastly, the cell area before and after the copy attempt provides the  $H_{area}$ term. Together, the net change in the Hamiltonian associated with that copy attempt, i.e.,  $\Delta H$ , provides the local energy for the cell before and after the copy attempt. Energetically favorable cell moves are always accepted, and to account for random motility, energetically unfavorable cell moves, i.e., copy attempts that increase the Hamiltonian, are accepted with Boltzmann probability,

$$P(\Delta H) = \begin{cases} 1, & \text{if } \Delta H < 0, \\ e^{-\Delta H/T}, & \text{if } \Delta H \ge 0, \end{cases}$$
 (14)

where T > 0 is a temperature term that captures intrinsic cell motility. Since cell–cell contacts are dynamic, the adjacency matrix A and thus traction and cell–cell junction forces are recalculated after each MCS.

Key model parameters are given in Table S1, and unless otherwise stated, simulations utilize parameter values established by van Oers et al. (2014). Parameter studies were performed with different combinations of cell–cell interaction energies and cell–matrix interaction energies,  $J_{\rm cc}$  and  $J_{\rm cm}$ , respectively, each repeated with a uniquely seeded random number to account for simulation randomness. The confluence is determined by the ratio of total cell-occupied pixels to the total grid area. The cell area is the number of pixels occupied by each unique cell state, and the cell count is the number of unique states. Simulations were numerically integrated in MATLAB v2018a (MathWorks, Natick, MA).

# 2.7 Cells and reagents

Human MCF10A mammary epithelial cells were obtained from the National Cancer Institute Physical Sciences



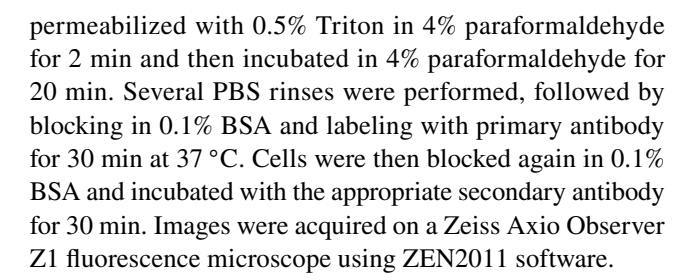
in Oncology Bioresource Core Facility, in conjunction with American Type Culture Collection (Manassas, VA). Madin-Darby Canine Kidney (MDCKII) cells were a gift of Rob Tombes (VCU). All cells were cultured in a humidified atmosphere at 37 °C with 5% CO<sub>2</sub>. MCF10As were maintained under standard culture conditions in DMEM/F-12 HEPES (Life Technologies, Carlsbad, CA), supplemented with 5% horse serum, 0.05% hydrocortisone, 0.01% cholera toxin, 0.1% insulin, 0.02% EGF and 1% antibiotics. MDCKII cells were maintained under standard culture conditions in DMEM (Life Technologies, Carlsbad, CA) supplemented with 10% fetal bovine serum and 1% antibiotics. Purified recombinant active TGF-β1 was purchased from Sigma-Aldrich (St. Louis, MO). Immunofluorescence imaging was conducted using the following primary antibodies: Ms anti-Hu E-cadherin (HECD-1, Abcam, Cambridge, UK), Ms anti-Ms N-cadherin (BD Biosciences, San Jose, CA), Rb anti-Hu FN (Abcam, Cambridge, United Kingdom), Ms anti-Hu LTBP-1 (RD Systems, Minneapolis, MN), Rb anti-Hu Smad2 (86F7, Cell Signaling Technology, Danvers, MA), and Dapi (Thermo Fisher Scientific, Waltham, MA). F-actin images were acquired by labeling cells with Alexa Fluor 555 Phalloidin (Life Technologies, Carlsbad, CA).

# 2.8 Microcontact printing

Microcontact-printed square islands were generated as previously described (Tan et al. 2004). Briefly,  $250 \,\mu\text{m} \times 250 \,\mu\text{m}$ squares were constructed by generating a negative mold template on a silicon wafer made from an epoxy-type, near-UV photoresist (SU-8; Microchem) using traditional photolithographic techniques. A replica mold of poly(dimethylsiloxane) (PDMS; Sylgard 184, Fisher Scientific, Hampton, NH) raised patterns was coated with 100 μg/ml laminin (Sigma-Aldrich, St. Louis, MO) for 2 h at 37 °C. Stamps were then rinsed in dH2O and dried with nitrogen gas. The laminin square islands were then stamped onto a thin layer of UV-treated PDMS on top of a glass coverslip. 2% Pluronics F-127 in phosphate-buffered saline (PBS) was used to prevent cells from adhering outside of the laminin-stamped areas. Coverslips were rinsed in PBS prior to cell seeding. Efficiency of protein transfer was confirmed by immunofluorescence labeling of the extracellular matrix protein.

### 2.9 Immunofluorescence microscopy

MCF10As or MDCK II cells  $(0.5 \times 10^6)$  were plated on  $250 \,\mu\text{m} \times 250 \,\mu\text{m}$  microcontact-printed square islands coated with  $100 \,\mu\text{g/mL}$  laminin. Cells were cultured for 18 h and were then transferred to EGF- and serum-free culture conditions for 2 h. Cells were then incubated with TGF- $\beta$ 1 (0, 2, 4 ng/mL) and cultured for an additional 48 h. Cells were



# 2.10 Cell area and cell number quantification

Cell area and cell number were determined by analyzing immunofluorescence images of F-actin and nuclei via a custom-written image processing algorithm in MATLAB. Binary masks of nuclei were generated by thresholding grayscale nucleus images; objects in the binary mask were counted to determine total cell number. To determine cell size, the centroid of each object in the binary mask was determined using the regionprops function. Nuclei centroids were used to generate a Voronoi diagram, which consists of a series of polygons that have edges that are equidistant from neighboring nuclei. Previous studies have demonstrated that Voronoi diagrams reasonably predict cell boundaries in an epithelial monolayer (Bock et al. 2010) and provide a more consistent quantification of cellular size as opposed to quantification of protein markers in the cell-cell junction, whose expression and localization change as TGF- $\beta$ 1 dose increases. Cell area was calculated for each cell by summing the pixels in each Voronoi polygon and was averaged across the 250  $\mu$ m  $\times$  250  $\mu$ m colony. Spatial localization of cell number and cell area was determined by binning nucleus centroids into a  $5 \times 5$  grid. Cell counts in each bin were totaled, and cell areas for each bin were averaged if the nuclei centroid was contained within the bin. Spatial localization data were further combined into either corner bins, edge bins, or interior bins, such that there was no overlap between the three regions (i.e., corner bins were not included in the edge region).

# 2.11 FRET analysis

To measure force on cell-cell junctions, fluorescence resonance energy transfer (FRET)-based, full-length E-cadherin tension biosensors were stably transfected into MDCK II cells. Epithelial square islands were cultured as stated above, and images were acquired on a Zeiss LSM 710 laser scanning microscope using ZEN2011 software. Briefly, mTFP (donor) and mEYFP (acceptor) fluorophores were imaged utilizing spectral unmixing at 458-nm excitation. The acquired intensity images were manually masked through ImageJ. Background subtraction and removal of saturated pixels were then performed via an image processing algorithm in Python as previously described (Arsenovic et al.



2016). FRET ratio was determined by obtaining the acceptor/donor ratio and multiplying with a binary mask of the junctions. This allowed for inspection of FRET pixels of interest within outlined cell–cell junctions.

## 2.12 Statistical analysis

Simulated and experimental data were exported to Prism 8 (GraphPad Software Inc.) for analysis. Statistical significance, indicated by a p value less than 0.05, was determined by one-way ANOVA across each TGF- $\beta$ 1 dosage, ratio of interaction energies, and/or spatial localization.

## 3 Results

# 3.1 Multicellular traction forces drive formation of epithelial monolayers

Prior studies from van Oers, Rens, and colleagues demonstrated that a hybrid CPM–FEM model can predict cellular spreading and organization based on cell-generated traction forces, resulting strains in the substrate, and durotaxis-driven migration in the CPM. To expand this model to adherent cell

monolayers, we incorporated several advancements: First, cellular traction forces were predicted from the FMA model (Lemmon and Romer 2010) based on a cell cluster geometry, not on individual cells. As such, cells in contact with neighboring cells "adhere" and begin to generate traction forces as a cohesive unit. Second, we assume that each cell in a multicellular cluster still maintains a static equilibrium, as has been suggested previously (Liu et al. 2010). As such, we require the force acting on cell–cell junctions to counter the net traction force for each cell, as illustrated in a simple two-cell example (Fig. 1c, left).

Figure 1 depicts simulated non-proliferating cells (red pixels) with corresponding scaled substrate strains (black vectors) for two scenarios. In the first, traction force is calculated from the first moment of area (FMA) about the single cell geometry, and each cell is in static equilibrium. As a result, the net imbalance for each cell is zero and no force is transferred across the cell–cell junction (Fig. 1a, Movie S1). In the second scenario, traction force is calculated from FMA about the multicellular geometry and each *cluster* is in static equilibrium (Fig. 1b, Movie S2). The net force imbalance for each cell is balanced by the intercellular tension, which transfers the traction force to neighboring cells. Without redistribution of cytoskeletal stress to neighboring cells

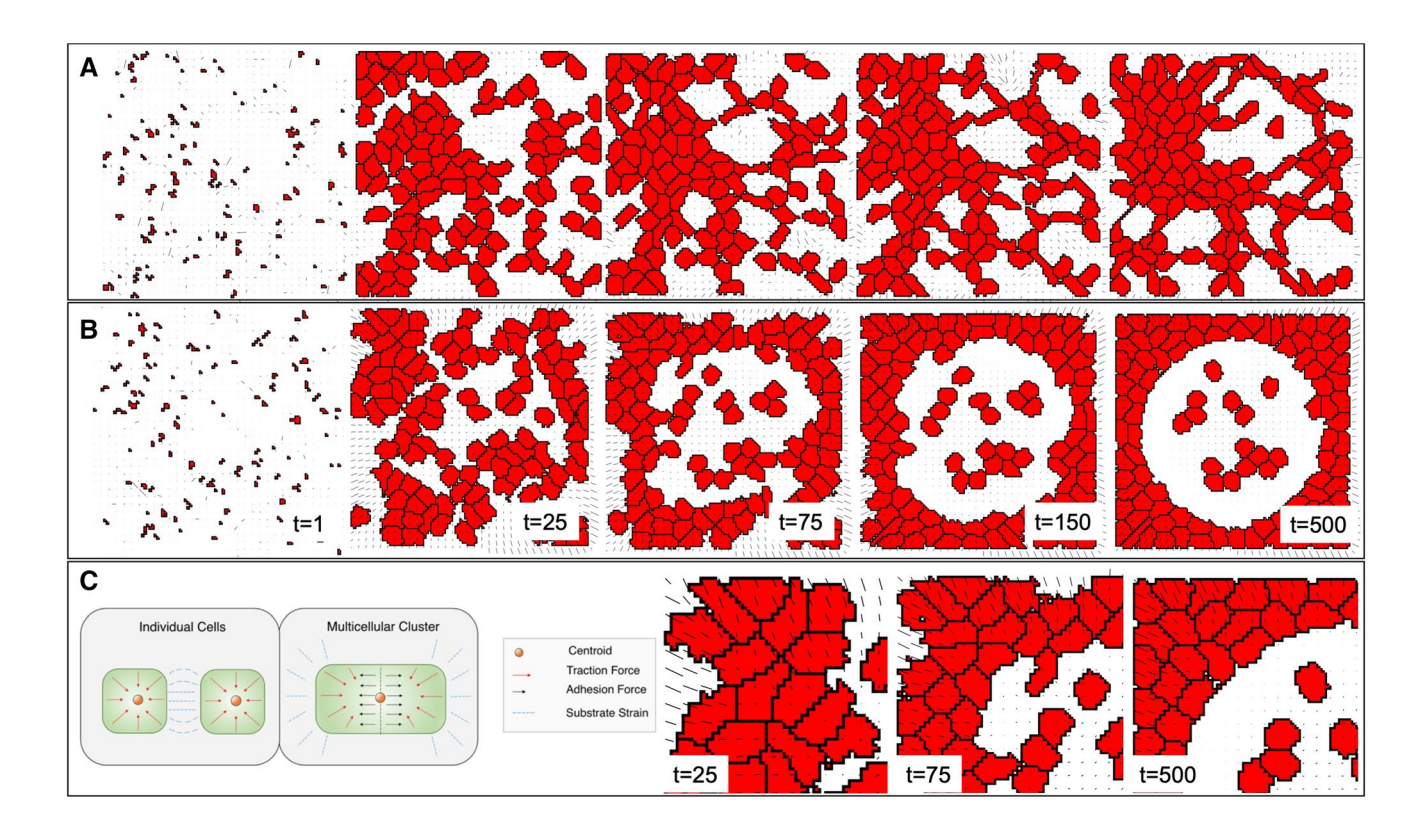


Fig. 1 Simulated cells (red pixels) migrate on a finite element substrate that responds to cell-generated traction forces. Traction forces are calculated based on either  $\bf a$  individual-cell geometries or  $\bf b$  multicellular clusters.  $\bf c$  (left) Representation of traction forces with result-

ing strain for multicellular geometries, and  ${\bf C}$  (right) inset of time points from  ${\bf b}$ . Time in units of Monte Carlo steps (MCS). Proliferation rate  $p_{divide}=0$  for this figure only



across cell-cell junctions, cellular alignment is localized and multicellular structures behave as partially cooperative networks with discordant substrate strains (Fig. 1a), as demonstrated by van Oers et al. (2014). In contrast, traction force distribution across cell-cell junctions to neighboring cells results in highly cooperative networks with a uniform spatial gradient of substrate strains. The formation of these cohesive multicellular clusters resembles an epithelial monolayer with preferential localization toward the boundary (Fig. 1b). In the resulting multicellular clusters, net traction forces have a magnitude and direction at any given point proportional to the FMA about that point in the cluster, resulting in a linear gradient of substrate strain oriented radially toward the cluster centroid (Fig. 1c, right, Fig S2).

# 3.2 Spatiotemporal dynamics of monolayer confluence

Preliminary simulations demonstrated the formation of a subconfluent monolayer-like sheet, which alters the spatial distribution of monolayer stress. To reproduce the spatiotemporal dynamics of an in vitro epithelial monolayer, specifically monolayer confluence, we incorporated cellular proliferation into the CPM to account for cell division dynamics and then compared the spatiotemporal dynamics with cultured epithelial cells (Fig. 2). Mammary breast epithelial cells (MCF10A) were seeded onto poly(dimethylsiloxane) (PDMS) substrates with a 250  $\mu m \times 250 \,\mu m$  microcontact-printed area of laminin (Fig. 2a, Movie S3). Epithelial monolayers reached confluence over approximately 24 h. Simulated cells exhibit similar patterning representative of MCF10A confluence dynamics (Fig. 2b, Movie S4). To estimate the rate of proliferation in the simulations, immunofluorescence images were analyzed at 0, 6, 12, 18, and 24 h and quantified for confluence as a function of time (Fig. 2c). We compare the half maximal confluence for simulations and experiments in order to estimate that 1 Monte Carlo step (MCS) corresponds to approximately 4.8 min of experimental time (Fig. 2b, c). The experimental timescale was used to estimate a simulated division probability of 0.5% per MCS. These results demonstrate that simulated spatiotemporal dynamics approximate cellular dynamics observed in vitro and agree with previous studies (Puliafito et al. 2012).

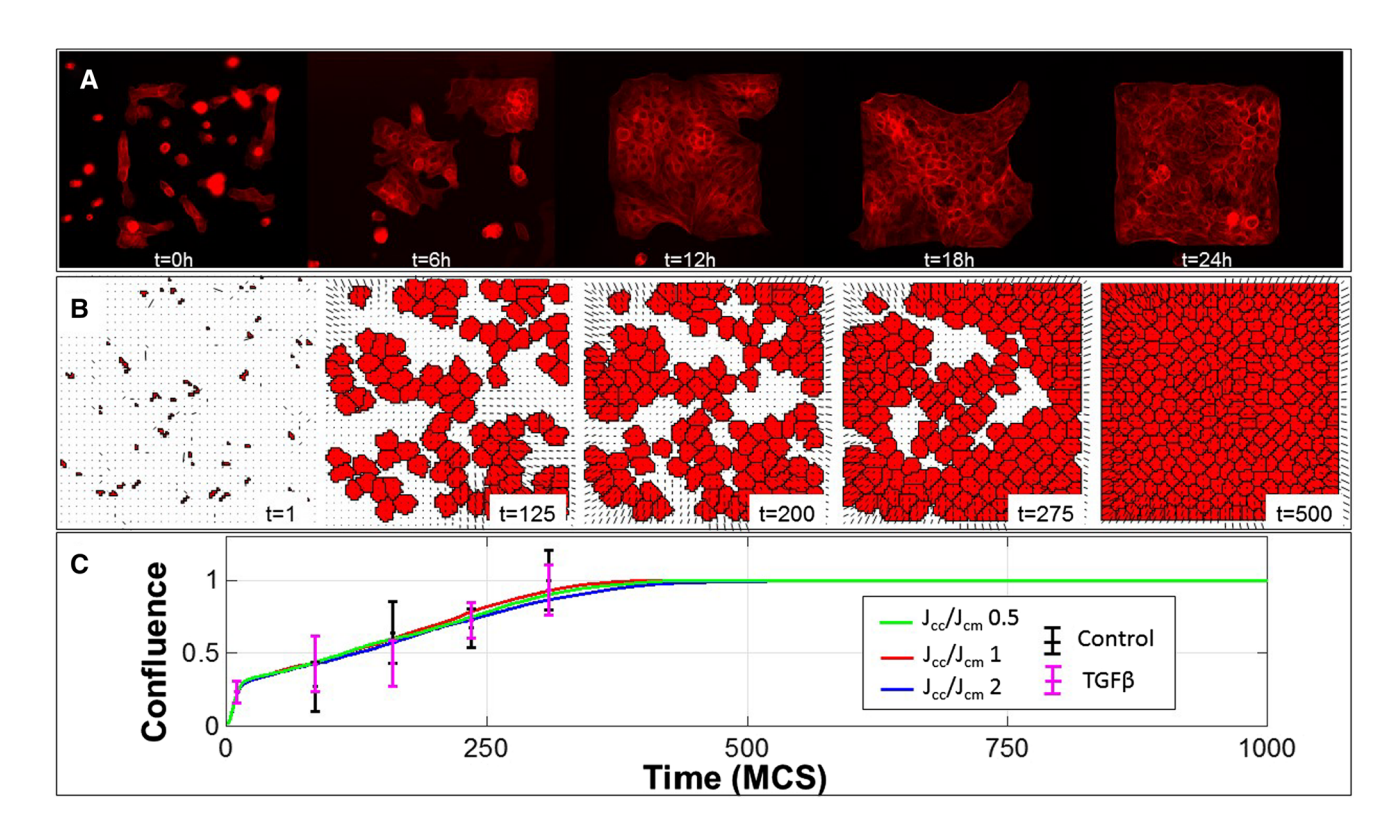


**Fig. 2** Spatiotemporal dynamics of simulated and in vitro tissue patterning. Visual comparison of time points from initial seeding to confluence illustrates parallels between **a** in vitro immunofluorescence images of actin (red) and **b** simulated spatial patterns. Time in panel A in hours, and in panel in Monte Carlo steps (MCSs). **c** Confluence, defined as the fraction of total cell area to total substrate area, is shown as a function of time, for in vitro and in silico experiments, for

different conditions: in silico measurements of confluence are shown for different values of the cell contact inhibition to substrate inhibition ( $J_{\rm cc}/J_{\rm cm}$ ; green, red, blue lines). In vitro mean confluence measurements  $\pm$  standard error are shown for control (black) and 4 ng/mL TGF- $\beta$ 1 treatment (magenta). Timescale relating in vitro to in silico measurements: 4.8 min/1 MCS,  $J_{\rm cm}=2.5$ 



# 3.3 Decreasing contact inhibition increases cell size and decreases cell number in confluent monolayers

With the key addition that traction forces are governed by the FMA model about the cluster geometry rather than the single cell geometry, the previous results illustrate distinct spatial patterning representative of epithelial monolayers. We next utilized our model to simulate epithelial monolayer and associated EMT-like dynamics. One key aspect of the epithelial phenotype is contact inhibition, that is, the propensity of a cell to stop migration when a neighboring cell is encountered (Mendonsa et al. 2018; Scarpa et al. 2015). As epithelial cells undergo phenotypic changes associated with EMT and become more mesenchymal-like, contact inhibition is reduced (Carmona-Fontaine et al. 2008). To mimic the effects of these phenotypic changes in epithelial monolayers in our multicellular FMA model, we varied the relative interaction energies between neighboring cells in the CPM, which simulates changes in contact inhibition. We varied the ratio of interaction energies at the cell-cell and cell-matrix interfaces,  $J_{\rm cc}$  and  $J_{\rm cm}$ , respectively (see Materials and Methods, Eq 3), for the single cell (Fig. 3a-d) and multicellular (Fig. 3e-h) FMA models. The magnitude of the respective energies represents a prohibitive interaction, i.e., a lower  $J_{cc}/J_{cm}$  ratio reflects lower cell-cell contact inhibition between adjacent cells. For each simulation, we measured the steady-state monolayer confluence, average cell area, total cell count, and relative net cellular traction forces, averaged over 5 simulations with distinct random cell seeding, and plotted these measures as a function of the  $J_{\rm cc}/J_{\rm cm}$  ratio. These simulations were then repeated for 3 distinct values of cell–matrix interaction energies,  $J_{\rm cm}$ .

Results indicate similar trends between the single cell and multicellular FMA models, with the exception of net cellular traction force, which equals zero by design for a cell in static equilibrium in the single cell FMA model (Fig. 3d). Beyond a critical point ( $J_{\rm cc}/J_{\rm cm}=2$ ), high cell–cell contact inhibition precludes the formation of confluent monolayers (Fig. 3a, e). We note that for even larger values of the  $J_{\rm cc}/J_{\rm cm}$  ratio, non-physiological conditions arise in which high contact inhibition prevents all cell–cell contacts and all cells remain completely isolated.

Below this critical point (i.e.,  $J_{\rm cc}/J_{\rm cm} \leq 2$ ), we find that the time course of monolayer confluence only weakly depends on cell contact inhibition (Fig. 2c). Further, for these conditions that form confluent monolayers, increasing cell–cell contact inhibition results in smaller cell area (Fig. 3b, f) and higher cell count (Fig. 3c, g). In the multicellular FMA model, the mean net traction force per cell weakly decreases as the  $J_{\rm cc}/J_{\rm cm}$  ratio increases (Fig. 3h), while for all parameter conditions, there is large variability in the net traction force due to the strong dependence on spatial location that arises in the multicellular FMA. We find

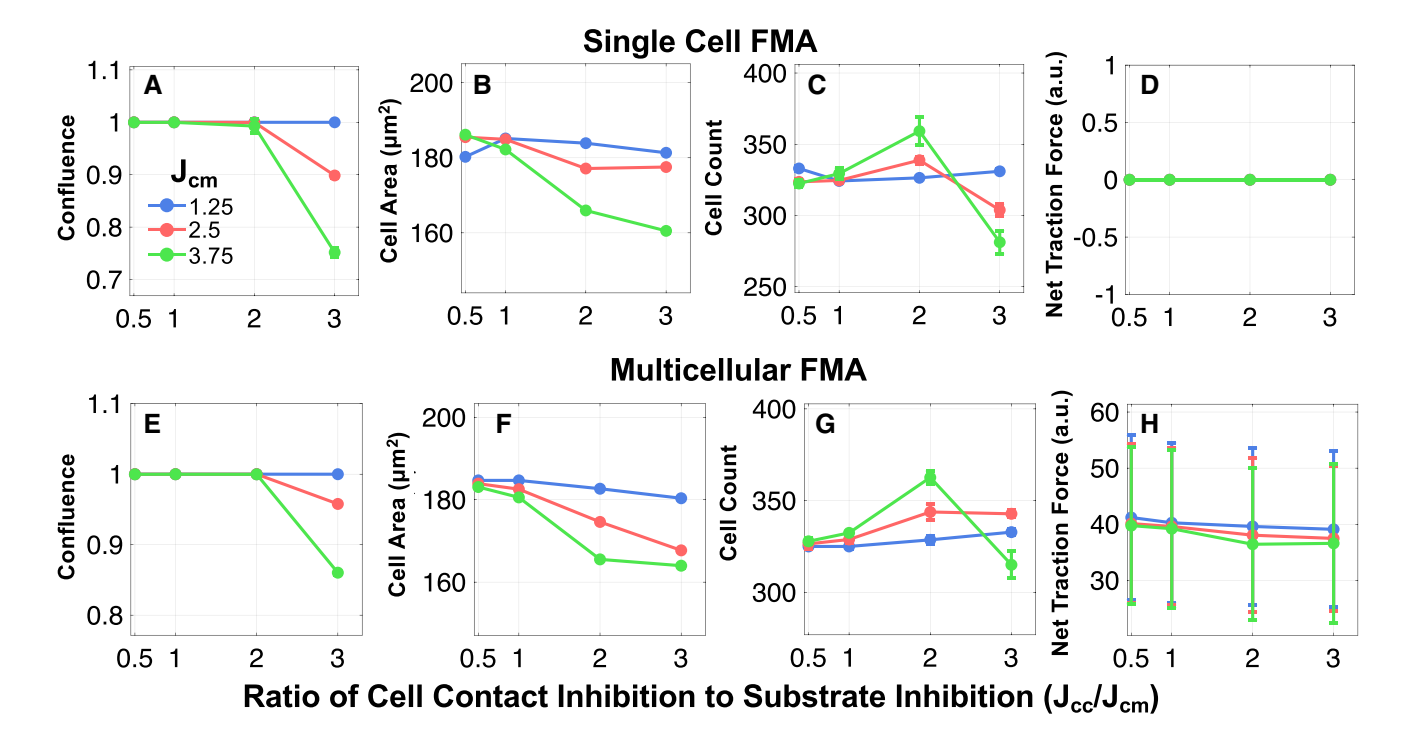


**Fig. 3** Parameter sweep of interaction energies. **a-d** Single cell first moment of area (FMA) model and **e-h** multicellular FMA-simulated confluence, cell area, cell count, and net traction force, shown as a

function of the ratio of cell–cell contact inhibition to cell–matrix inhibition ( $J_{\rm cc}/J_{\rm cm}$ ), varying  $J_{\rm cm}$  values



that higher substrate inhibition, i.e., increased  $J_{\rm cm}$ , tends to increase the sensitivity to the  $J_{\rm cc}/J_{\rm cm}$  ratio for all measures. Thus, these data indicate that a loss of cell–cell contact inhibition leads to larger cells and lower cell count.

# 3.4 Decreasing simulated contact inhibition mimics TGF- $\beta$ 1-induced EMT

The above results suggest that cells in the multicellular FMA model resemble the archetypal phenotype of epithelial cells undergoing EMT. With decreased cell-cell contact inhibition (i.e., smaller  $J_{\rm cc}/J_{\rm cm}$  ratio), simulated cells exhibit increased spreading and decreased proliferation characteristic of the mesenchymal phenotype, while with increased cell-cell contact inhibition (i.e., larger  $J_{\rm cc}/J_{\rm cm}$  ratio), simulated cells exhibit decreased spreading and increased proliferation characteristic of the epithelial phenotype. Together, these results indicate that the  $J_{\rm cc}/J_{\rm cm}$  ratio may serve as a suitable comparison to in vitro models of growth factorinduced EMT. We thus compared these results to experiments in which EMT was induced by the soluble growth factor TGF- $\beta$ 1, as has previously been detailed (Lamouille et al. 2014). Representative immunofluorescence images of MCF10A cells treated with increasing dosages of TGF-β1 illustrate a phenotypic switch from cortical actin, which is typically observed in epithelial cells, to pronounced actin stress fibers associated with the mesenchymal phenotype (Fig. 4a). In these confluent monolayers, MCF10A average cell count decreases and average cell area increases for increasing TGF- $\beta$ 1 doses (Fig. 4b, d). As in Fig. 3, we observe similar trends in simulations for decreasing cell contact inhibition (i.e., smaller  $J_{\rm cc}/J_{\rm cm}$  ratio), although with a weaker dependence than observed in vitro (Fig. 4c, e). Thus, we find that cell contact inhibition similarly regulates the cellular geometry averaged over the confluent monolayer in both simulation and experiment.

# 3.5 Cell-cell junction force maintains mechanical equilibrium of multicellular clusters

A key advance of the multicellular FMA model is the prediction of forces acting on cell-cell junctions. By assuming static equilibrium and applying a force-balance principle, cell-cell junction force was predicted as a reaction force that balances traction forces of the monolayer. Cell-cell junction force magnitudes are shown on the boundaries between neighboring cells in simulated monolayers (Fig. 5d). To examine spatial trends, we segmented the simulation domain into a  $5 \times 5$  grid of bins and calculated the mean junction force magnitude within each bin (Fig. 5e). The spatial distribution of junction forces is pronounced, with the largest forces in the interior and smallest in the corners (Fig. 5f).

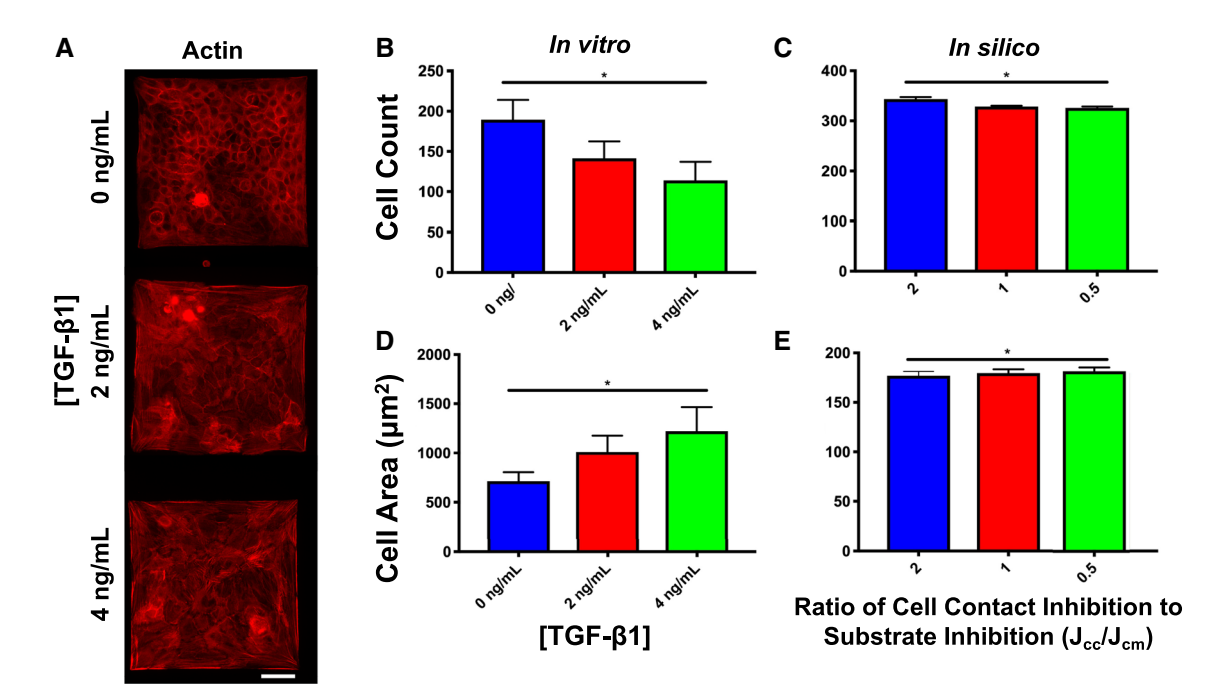


**Fig. 4** Morphological characterization of the epithelial tissues with altered contact inhibition. **a** Representative immunofluorescence images of actin (red) illustrate a confluent MCF10A monolayer bounded by the  $250 \times 250 \mu m$  microfabricated square; scale bar =  $50 \mu m$ . In vitro (**b**, **d**) and in silico (**c**, **e**) average cell count and cell area for the confined geometry are shown for each TGF-β1 dos-

age and ratio of contact interaction energies  $(J_{\rm cc}/J_{\rm cm})$ , respectively. Sample sizes: n=3 experiments, 7–10 monolayers per experiment per dose (in vitro); n=5 simulations per parameter set (in silico). \* denotes significance by one-way ANOVA test between each TGF- $\beta$ 1 dosage (**b**, **d**) or each contact energy ratio (**c**, **e**)



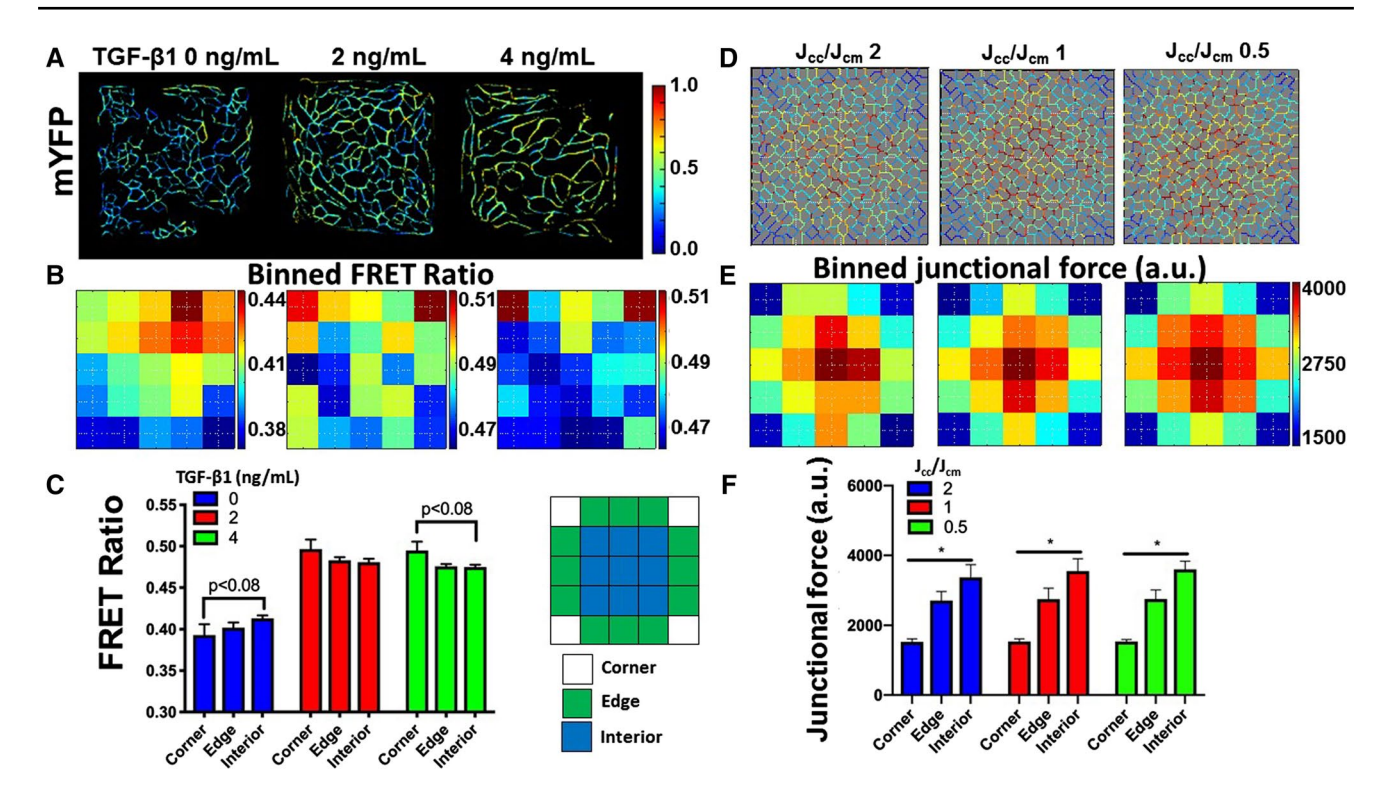


**Fig. 5** Simulated cell–cell junction force spatial patterns reflect TGF- $\beta$ 1 effects in vitro. **a** In vitro FRET intensities in MDCK II cells. **b** Corresponding heatmaps for average FRET intensities are binned into a 5 × 5 grid, and **c** their associated mean for corner, edge, and interior bins for 0, 2, and 4 ng/mL TGF- $\beta$ 1 dosages. Note the *y*-axis lower limit in panel C corresponds to a FRET ratio of 0.3. Schematic (right) illustrates bin positions. **d** Simulated cell–cell junction force is depicted as the net magnitude for high, medium, and low interaction energy ( $J_{cc}/J_{cm}$ ) ratios. **e** cell–cell junction force magnitudes are

shown as a  $5 \times 5$  grid with **f** their associated mean for corner, edge, and interior bins. Sample sizes: n = 3 experiments, 7–10 monolayers per experiment per dose (in vitro); n = 5 simulations per parameter set (in silico). Binned and position values shown in panels **b**, **c** and **e**, **f** represent averages over all samples. In panel **c**, p value denotes near significance for Student's t test comparing Corner and Interior spatial locations. \*Denotes significance by one-way ANOVA test between spatial location (**f**). Force in panels **d**, **e**, and **f** in arbitrary units (a.u.)

However, interestingly, we find minimal variation in the spatial trends between low, medium, and high contact inhibition ratios.

We next sought to compare these with experimentally measured junction forces. To measure cell-cell junction forces experimentally, MDCKII cells were stably transfected with a full-length E-cadherin force sensor, as previously described (Mohan et al. 2018). Briefly, the force sensor consists of two fluorophores coupled by a polypeptide that exhibits elasticity. The two fluorophores are designed such that, when in close proximity, the pair exhibits Forster resonance energy transfer (FRET), that is, emission light from the first fluorophore is absorbed by the second fluorophore, which emits light. As the sensor is stretched and the fluorophore pair moves apart, the excitation of the second fluorophore by the first fluorophore decays, resulting in a loss of FRET excitation relative to excitation of the first fluorophore. This force sensor was inserted into E-cadherin, which comprises the homophilic binding event in cell-cell junctions known as adherens junctions. Validation and functionality of this sensor have been previously demonstrated (Arsenovic et al. 2017; Borghi et al. 2012). Phenotypic changes associated with epithelial cells undergoing EMT were again induced by increasing dosage of TGF- $\beta$ 1 (Fig. 5a). FRET ratio reflects the energy transfer between the two fluorophores, in which FRET ratio is inversely proportional to tension on the FRET force sensor: High FRET ratio indicates low tension and low FRET ratio indicates high tension. Representative pseudocolored images of the processed FRET ratio are shown in Fig. 5a. We next investigated whether spatial patterns of junction forces were established in these confluent monolayers. We again segmented images of the local net FRET ratios into a 5  $\times$  5 grid. In the absence of TGF- $\beta$ 1, colonies illustrated a nearly spatially uniform low FRET ratio, indicating high cell-cell tension throughout the monolayer (Fig. 5b). TGF- $\beta$ 1 treatment increased FRET ratio, indicating a drop in overall intercellular tension. Additionally, a small spatial gradient was established, with higher FRET ratios (lower cell-cell tension) in the corner and edges and lower FRET ratios (higher cell-cell tension) in the interior of the monolayer, consistent with a spatial gradient of larger junction



forces in the center and decreasing toward the edges and corners (Fig. 5c).

Thus, we find that simulated cell–cell junction forces predict a spatial trend of decaying cell–cell tension from interior to periphery. Furthermore, simulated spatial gradients of cell–cell junction force are most comparable to experimental measures of TGF- $\beta$ 1-treated monolayers.

## 3.6 Individual cell geometry spatial patterns

Summarizing our results presented thus far, we find that the multicellular FMA model reproduces contact inhibition-dependent trends for average cellular geometry (i.e., cell size and count), but underestimates this dependence compared with experimental observations. Further, our model qualitatively predicts trends for spatial patterns of cell–cell junction forces in TGF- $\beta$ 1-treated monolayers, but overestimates the magnitude of the spatial gradient, in comparison with experiments. We hypothesize that these discrepancies arise from an underestimation of cell size distribution throughout the monolayer in response to changes in contact inhibition. That is, individual cell size changes in response to TGF- $\beta$ 1 treatment due not only to loss of cell contact inhibition, but also to additional signaling not currently present in our model. To

investigate this, we again segmented immunofluorescence images of MCF10A cells and binned cell area as before into a  $5 \times 5$  grid (Fig. 6a). Consistent with overall monolayer averages, cell area increased with increasing TGF- $\beta$ 1 dose. Evaluating the average cell area in the corner, edge, and interior of the monolayer reveals an overall increase in cell area at the periphery of the square, with the largest cell area localized to the corners in both low and high TGF- $\beta$ 1 dosages (Fig. 6a). Reduced contact inhibition by treatment with TGF- $\beta$ 1 accentuates this trend, resulting in a large spatial gradient in cell area (Fig. 6b).

In contrast, simulated cell area exhibited substantially reduced spatial variation compared to experimental cell area (Fig. 6c). Furthermore, the effects of contact inhibition had a relatively minimal effect on spatial variation of cell area, resulting in slightly increased cell area at the monolayer interior (Fig. 6d). Thus, the lack of accounting for heterogeneous cellular properties, specifically cell area, is a key limitation of our model. Since cells undergo profound phenotypic changes throughout EMT, it would be reasonable that these changes lead to parameter changes within the CPM for each individual cell; incorporating these changes in cell phenotype into the CPM component is a primary future goal for the model development.

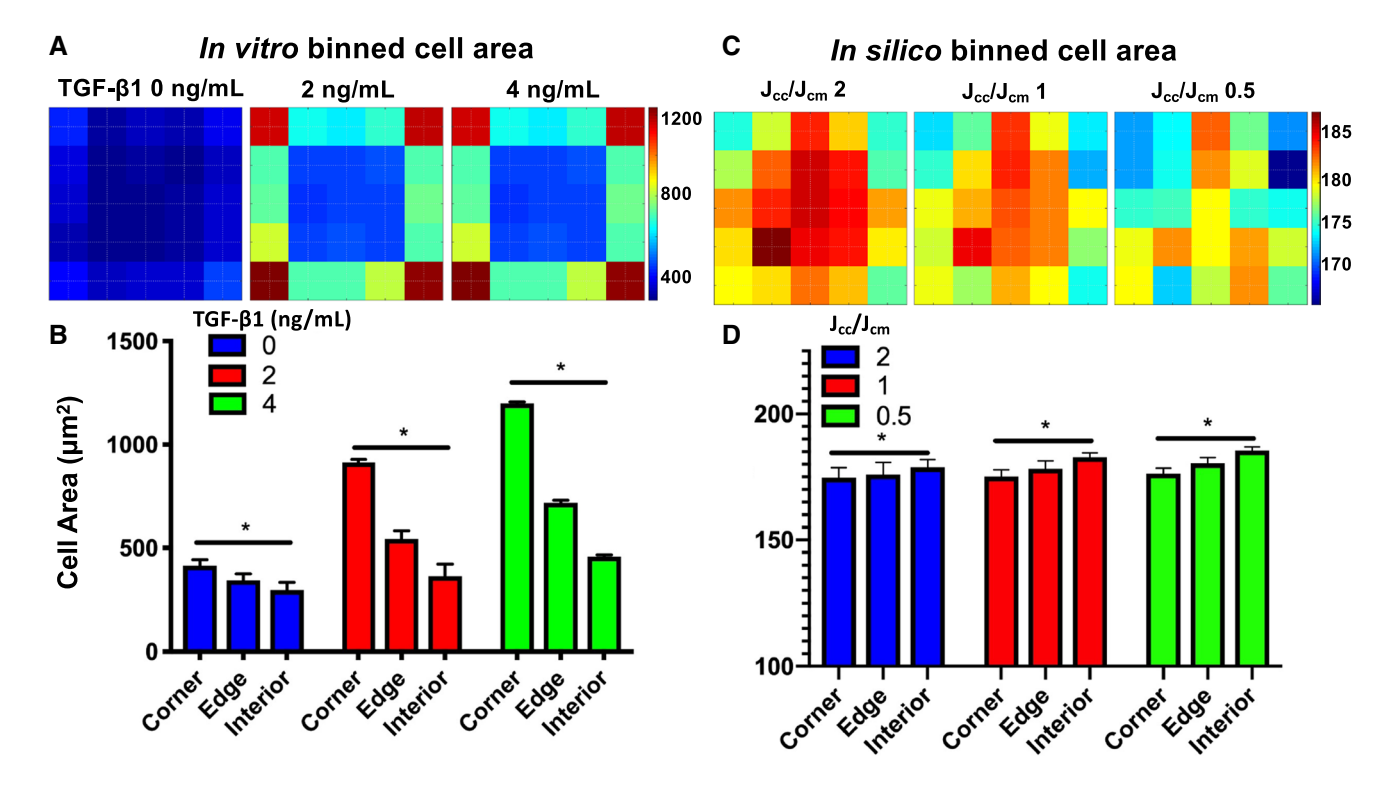


**Fig. 6** Individual cell geometry spatial patterns **a** In vitro heatmaps for binned cell area treated with 0, 2, and 4 ng/mL TGF- $\beta$ 1 and **b** their associated bar graphs for average corner, edge, and interior. **c** In silico heatmaps for binned cell area at high, medium, and low contact inhibition and **d** their associated bar graphs. Sample sizes: n = 3

experiments, 7–10 monolayers per experiment per dose (in vitro); n=5 simulations per parameter set (in silico). Binned and position values represent averages over all samples. \*Denotes significance by one-way ANOVA test between each spatial location ( $\mathbf{b}$ ,  $\mathbf{d}$ )



# 3.7 Analytical model of a simplified one-dimensional geometry

Both experimental and simulation data indicate that while traction forces are largest at the periphery of the epithelial cluster, junction forces are largest near the center of the clusters and decay toward the periphery. We can gain additional insights by considering junction forces in tissue with a simple one-dimensional geometry, to both illustrate our approach and explain the perhaps counterintuitive prediction that larger traction forces at the periphery result in larger junction forces at the center. For this simple geometry, the traction and junction force magnitudes can be solved analytically, and further, these analytical results provide an explanation for some of the discrepancies between experiments and simulations noted above.

Consider a linear array of 2n cells of length L that are arranged and coupled in a line, such that the cell-cell junctions are located at positions  $(-nL, 0), (-(n-1)L, 0), \ldots, ((0,0), \ldots, ((n-1)L, 0), (nL, 0),$  and define T = nL as the length of half of the monolayer or tissue (Fig. 7c). Note that the y position is insignificant, since all forces are oriented in the x-direction. The centroid of the cell

cluster aligns with the origin, (0, 0), which is the junction on the left edge of cell 1, and thus, the net traction force in each cell will be pointed toward this position. Further, we assume that each cell has f focal adhesions, uniformly spaced along the length of the cell L, and that traction forces are generated only at the focal adhesion positions. In the illustrated example, f = 4.

The magnitude of traction forces generated at each focal adhesion are thus proportional to the distance from the origin, and the net traction force for a given cell is the sum of all traction forces over all focal adhesions. We can show that for cell k, with left edge at position ((k-1)L, 0)and right edge at position (kL, 0), the net traction force is given by  $\vec{T}_k = (-\mu L f(k - \frac{1}{2}), 0)$ , where  $\mu$  is the appropriate scaling factor that relates cell geometry to traction forces (Lemmon and Romer 2010). For the rightmost cell, cell n,  $\vec{T}_n = (-\mu L f(n - \frac{1}{2}), 0)$ . For mechanical equilibrium at cell n, this traction force must be balanced by the junction force from cell n-1 to cell n, i.e.,  $\vec{T}_n + \vec{J}_{n,n-1} = 0$ , such that  $\vec{J}_{n,n-1} = (\mu L f(n-\frac{1}{2}), 0)$ . By assumption, net forces at the cell-cell junction are also in equilibrium, such that junction force pairs are symmetric, i.e., equal in magnitude and opposite in direction, and thus  $\vec{J}_{n-1,n} = (-\mu L f(n-\frac{1}{2}), 0)$ .

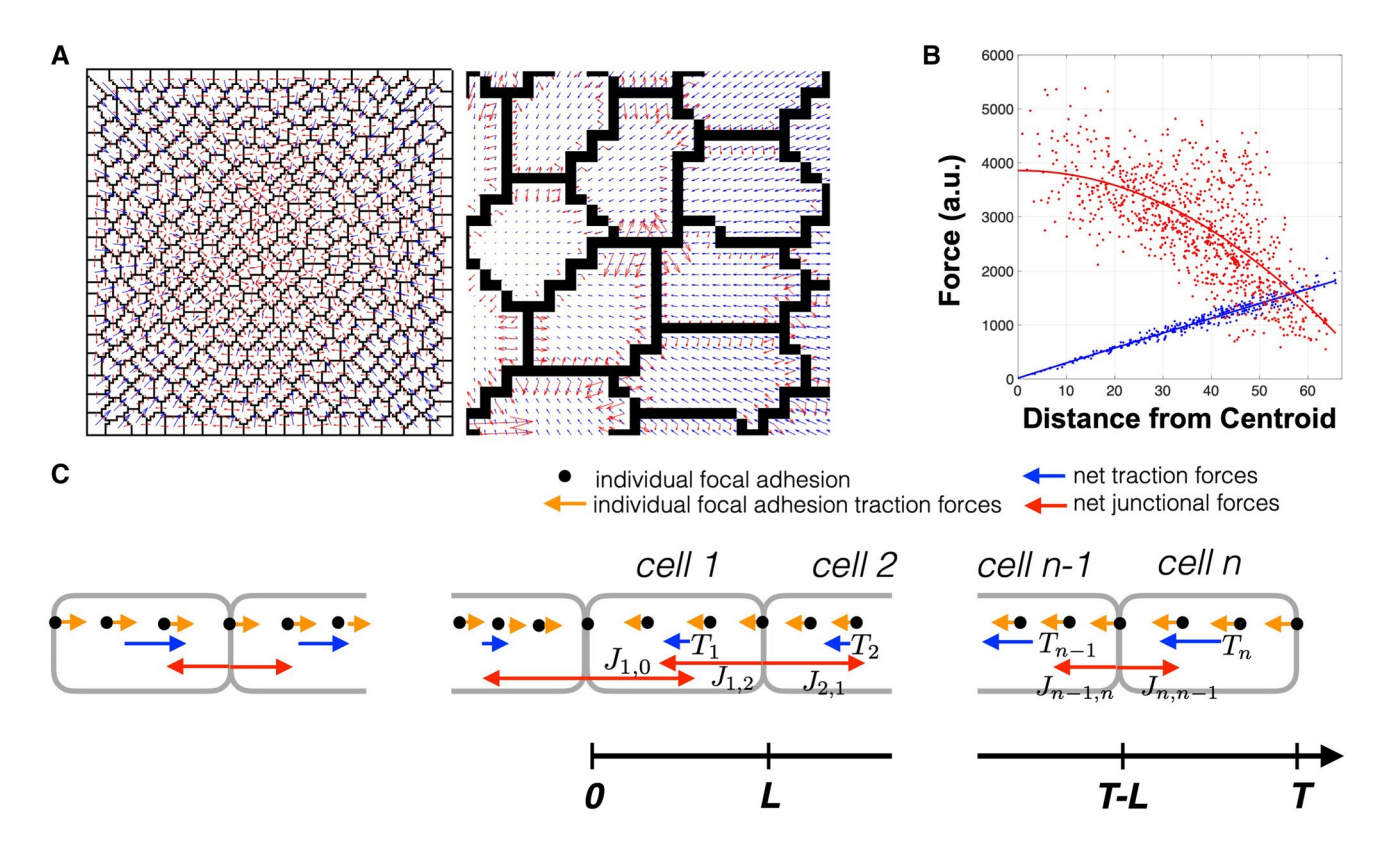


Fig. 7 Multicellular forces at mechanical equilibrium. a Representative snapshot of the traction and junction forces in the multicellular CPM model. b Plots of the traction and junction forces (in arbitrary units, a.u.) from the CPM simulations show that traction force (blue lines, circles) scales linearly with distance from monolayer centroid

and cell–cell junction forces (red line, circles) drop off quadratically from the centroid. c One-dimensional tissue simplification illustrating the balance of traction and cell–cell junction forces. See text for further description



Next considering forces on cell n-1, the junction force from cell n-2 to cell n-1 must balance both the net traction force  $\vec{T}_{n-1}=(-\mu L f((n-1)-\frac{1}{2}),0)$  and junction force  $\vec{J}_{n-1,n}$ , i.e.,  $\vec{T}_{n-1}+\vec{J}_{n-1,n}+\vec{J}_{n-1,n-2}=0$ , such that  $\vec{J}_{n-1,n-2}=(\mu L f(2n-2),0)$ . Similarly, junction force from cell n-3 to cell n-2,  $\vec{J}_{n-2,n-3}=(\mu L f(3n-\frac{9}{2}),0)$ . In general, we can show that the intercellular tension from cell k to k+1.

$$\vec{J}_{k+1,k} = \left(\frac{1}{2}\mu L f(n^2 - k^2), 0\right) = \left(\frac{1}{2}\mu f\left(\frac{T^2}{L} - Lk^2\right), 0\right). \tag{15}$$

Thus, the junction force at the cluster center, i.e., the left edge of cell 1,  $\vec{J}_{1,0} = (\mu L n^2 f/2, 0) = (\mu T^2 f/(2L), 0)$ . This simple geometry arrangement predicts larger magnitude junction forces in the center and further illustrates a quadratic drop-off (due to the  $-k^2$  term in the magnitude of  $\vec{J}_{k+1,k}$ ) that is predicted as junction position k increases toward the periphery. A representative example of the CPM model illustrates the distribution of traction forces (blue) and junction forces (red) in a confluent monolayer (Fig. 7b) and both the linear increase in traction force magnitude from the monolayer centroid and the quadratic drop-off in junction force magnitude (Fig. 7b).

Thus, for a monolayer of a given size, i.e., fixed T, Eq. 15 predicts that for a smaller cell size (decreased L and thus increased n), the magnitude of junction forces is larger throughout the monolayer, which is consistent with experimental measurements of lower FRET ratios (i.e., higher tension) in non-treated epithelial monolayers (Fig. 5c). Further, in TGF- $\beta$ 1-treated monolayers, more mesenchymal-like larger cells at the monolayer periphery would be expected to have more focal adhesions per cell, in contrast to epitheliallike smaller cells in the interior. Additionally, while larger cells at the periphery will reduce junction forces locally, due to the cumulative nature of junction forces required to maintain mechanical equilibrium originating at the periphery, this local reduction in junction forces would be expected to have a greater influence on interior junction forces. All of these considerations would be predicted to reduce the magnitude of the spatial gradient, also consistent with smaller spatial gradients observed experimentally. Thus, we expect that our future work incorporating spatial variations in cell size in the CPM model will more accurately reproduce experimental results.

We can further generalize this example and consider the continuous limit in the spatial dimension, in which the traction forces  $\tau(x)$  in the *x*-direction at position x (for x > 0) are given

$$\tau(x) = -\mu \phi(x)x,\tag{16}$$



where  $\phi(x)$  is the spatial distribution of focal adhesions per unit length. Junction forces J(x) at position x are then by definition the *second moment of area*, evaluated from the cluster periphery T to position x, where again x = 0 corresponds to the cluster center,

$$J(x) = \int_{T}^{x} \tau(\xi) d\xi = -\mu \int_{T}^{x} \phi(\xi) \xi d\xi.$$
 (17)

For uniform focal adhesion distribution,  $\phi(x) = f/L$ , we can integrate Eq. 16, and using the relationship x = kL, the result is equivalent to Eq. 15.

#### 4 Discussion

In this study, we illustrate a generalized framework for predicting the spatial distribution of forces within and between cells in a monolayer. By assuming that i) clustered epithelial cells act as a syncytial unit and generate forces collectively in the FMA model and ii) each cell in a monolayer exists in a quasi-equilibrium, in which junction forces and traction forces are balanced, we are able to predict the distribution of cell-cell junction forces and cell traction forces within an epithelial cluster. Our model demonstrates that traction forces scale with the size of the multicellular cluster, a consequence of the FMA in which traction force is applied at uniformly distributed cell-matrix adhesions (i.e., at all nodes in the CPM). The model further predicts that the intercellular tension decays nonlinearly with the distance from the monolayer center. FRET analysis of TGF- $\beta$ 1-treated epithelial clusters indicates junction force distribution depends on monolayer geometry and not individual cell geometry and confirms trends observed in simulations.

Many prior computational approaches have been developed to study tissue mechanical homeostasis, cellular migration, and cell-matrix interactions. Vertex-based mechanical models, which consider mechanical force-balance along the boundaries of cells accounting for active and passive mechanical forces, have been developed to model tissuescale emergent dynamics such as morphogenesis and migration (Okuda et al. 2015; Mathur et al. 2018; Du et al. 2014; Oelz et al. 2019; Bui et al. 2019). Agent-based models have been utilized to study cellular remodeling in response to mechanical perturbations, such as infarcts and wound healing (Richardson and Holmes 2016; González-Valverde and García-Aznar 2017; Lee et al. 2019). The CPM framework has also been utilized to study cell-matrix interactions via extracellular matrix remodeling, in settings such as metastatic cancer cell migration and angiogenesis (Edalgo et al. 2019; Daub and Merks 2013; Szabó and Merks 2013).

Our work builds on prior studies from Merks and colleagues that have demonstrated how local mechanical interactions can drive global cellular patterning and structure, using a hybrid CPM-FEM framework (van Oers et al. 2014; Rens and Merks 2017, 2019). Multiscale modeling studies from Chaplain and colleagues have predicted that junction forces are redistributed as cells form colonies, which in turn can drive intracellular signaling pathways (Schlüter et al. 2015; Ramis-Conde et al. 2008, 2009). Interestingly, our extension to including multicellular mechanical interactions demonstrates that a gradient of intercellular tension can form even in the absence of heterogeneous cell populations. Through transduction of the mechanical gradient to intracellular signaling pathways, this tension distribution can provide positional information within a monolayer that regulates cellular phenomena, such as cell growth, proliferation, and migration. This is of particular interest to spatial regulation of EMT, during which cell stress is distributed to the monolayer periphery (Gomez et al. 2010). Connecting biochemical and mechanical signaling, the dependence on E-cadherin further suggests that intercellular tension may serve as a predictor of EMT.

#### 4.1 Limitations and future considerations

The trends of our extended multicellular FMA model capture many key dynamical properties of epithelial monolayers undergoing EMT; however, the model does not fully capture all aspects of this transition. In particular, we noted above that simulated spatial gradients of cell-cell junction force based on the multicellular FMA model are most comparable to experimental measures of TGF- $\beta$ 1-treated monolayers, and not as comparable to the non-treated epithelial monolayers. The one-dimensional analytical model provides some possible insight into the source of model and experiment discrepancy. In the simplified geometry of the one-dimensional tissue, junction forces are predicted to decrease from the tissue center (see Eq. 15) and thus inconsistent with the near uniform distribution observed in non-treated epithelial tissue. While this general conclusion need not strictly hold in the two-dimensional setting, nonetheless, it suggests that the multicellular FMA model may not strictly hold for epithelial tissues. This is a key insight, as it suggests that there is a transition that occurs during EMT in the properties governing tissue mechanical equilibrium, in which the multicellular FMA model becomes appropriate. This would be consistent with experimental observations of a redistribution of mechanical forces that occurs during EMT as well. This transition in tissue-scale properties is complicated by the associated phenotypic changes that occur throughout EMT at the individual cell level. Our study importantly demonstrates both the agreement and discrepancies between experimental results and model predictions for tissues before and undergoing EMT and thus suggests sources for model improvement that are the focus of ongoing work.

While one additional possible source of experimental discrepancy is the utilization of different cell lines for cell geometry and FRET analysis, respectively, in general, we expect similar responses between the two epithelial cell lines. However, we note that the lack of agreement between model and experiment is itself an important and meaningful result, in particular a result that facilitates identifying aspects of the model that require refining and improvement. The observed differences between simulations and experiments may be due to a number of factors, including non-uniformity in cellular phenotype that in turn alters cell size and adhesion properties; changes in focal adhesion distribution that in turn alter traction forces; the number of cell-cell and cell-matrix attachments, as contacts between neighboring cells, is not fixed and may vary; and properties governing mechanical equilibrium, as noted above.

A defining characteristic of TGF- $\beta$ 1-induced EMT is the disassembly of epithelial junctions, resulting in the loss of contact inhibition. During this process, intercellular tension redistributes from the cell-cell junctions to the cell-matrix attachments, which allows for increased mobility, growth, and spreading (Scarpa et al. 2015). Our model represents this shift by altering contact penalties within the cell-cell and cell-matrix interaction energies. By altering the cell-cell contact energy, the model captures the contact inhibition of neighboring cells in vitro. However, simulating EMT via changes in the contact energy is not sufficient to capture all dynamics; in particular, simulations do not reproduce spatial patterns in cell area. In the CPM model, a defined value for optimal cell area constrains the simulated cell area that, in turn, limits cell-matrix adhesion. The shift from cell-cell contact to cell-matrix adhesion is indirectly restricted as a result. The spatial distribution of intercellular tension therefore predicts the spatial distribution of cell area, which would seem to indicate a shift toward cell-matrix adhesion. An ongoing focus of work is to incorporate variable cellular properties into the CPM to incorporate the effects of EMT progression on cell geometry and resulting spatial patterning in a more physiological manner.

Our model incorporates durotaxis into the Hamiltonian term of the CPM by assuming that cell-derived strain drives a strain-dependent increase in elastic modulus. This local, strain-dependent stiffening of the substrate is consistent with the viscoelastic nature of the PDMS substrates used here (unpublished results). However, the FEM component of the model assumes that the substrate is isotropically linearly elastic. This is computationally more direct, but does not account for either the viscoelastic nature of the substrates or the viscoelasticity of extracellular matrix (ECM) fibrils that are assembled by cells on top of the substrate. Future iterations of the model will explore how both viscoelastic effects of the substrate and anisotropic



and viscoelastic effects of the ECM alter cell size, traction force, and phenotype of cells in the simulations.

**Acknowledgements** The work was supported through funding from the National Institutes of Health R01GM122855 (SHW, CAL) and R35GM119617 (DEC).

### References

- Arsenovic P, Ramachandran I, Bathula K, Zhu R, Narang J, Noll N, Lemmon C, Gundersen G, Conway D (2016) Nesprin-2G, a component of the nuclear LINC complex, is subject to myosin-dependent tension. Biophys J 110(1):34. https://doi.org/10.1016/j.bpj.2015.11.014
- Arsenovic PT, Mayer CR, Conway DE (2017) SensorFRET: a standardless approach to measuring pixel-based spectral bleed-through and FRET efficiency using spectral imaging. Sci Rep 7(1):15609. https://doi.org/10.1038/s41598-017-15411-8
- Bazellières E, Conte V, Elosegui-Artola A, Serra-Picamal X, Bintanel-Morcillo M, Roca-Cusachs P, Muñoz JJ, Sales-Pardo M, Guimerà R, Trepat X (2015) Control of cell-cell forces and collective cell dynamics by the intercellular adhesome. Nat Cell Biol 17(4):409. https://doi.org/10.1038/ncb3135
- Bock M, Tyagi AK, Kreft JU, Alt W (2010) Generalized Voronoi tessellation as a model of two-dimensional cell tissue dynamics. Bull Math Biol 72(7):1696. https://doi.org/10.1007/s1153 8-009-9498-3
- Borghi N, Sorokina M, Shcherbakova OG, Weis WI, Pruitt BL, Nelson WJ, Dunn AR (2012) E-cadherin is under constitutive actomyosin-generated tension that is increased at cell-cell contacts upon externally applied stretch. Proc Natl Acad Sci 109(31):12568. https://doi.org/10.1073/pnas.1204390109
- Boudou T, Ohayon J, Picart C, Tracqui P (2006) An extended relationship for the characterization of Young's modulus and Poisson's ratio of tunable polyacrylamide gels. Biorheology 43(6):721
- Bui J, Conway DE, Heise RL, Weinberg SH (2019) Mechanochemical coupling and junctional forces during collective cell migration. Biophys J 117(1):170–183
- Carmona-Fontaine C, Matthews HK, Kuriyama S, Moreno M, Dunn GA, Parsons M, Stern CD, Mayor R (2008) Contact Inhibition of locomotion in vivo controls neural crest directional migration. Nature 456(7224):957. https://doi.org/10.1038/nature07441
- Daub JT, Merks RMH (2013) A cell-based model of extracellular-matrix-guided endothelial cell migration during angiogenesis. Bull Math Biol 75(8):1377. https://doi.org/10.1007/s11538-013-9826-5
- Du X, Osterfield M, Shvartsman SY (2014) Computational analysis of three-dimensional epithelial morphogenesis using vertex models. Phys Biol 11:066007
- Edalgo YTN, Zornes AL, Versypt ANF (2019) A hybrid discrete continuous model of metastatic cancer cell migration through a remodeling extracellular matrix. AIChE J 65(9):e16671
- Ettensohn CA (1985) Mechanisms of epithelial invagination. Q Rev Biol 60(3):289. https://doi.org/10.1086/414426 PMID: 3901078
- Fristrom D (1988) The cellular basis of epithelial morphogenesis. A review. Tissue Cell 20(5):645. https://doi.org/10.1016/0040-8166(88)90015-8
- Gomez EW, Chen QK, Gjorevski N, Nelson CM (2010) Tissue geometry patterns epithelial-mesenchymal transition via intercellular mechanotransduction. J Cell Biochem 110(1):44. https://doi.org/10.1002/jcb.22545

- González-Valverde I, García-Aznar JM (2017) A hybrid computational model to explore the topological characteristics of epithelial tissues. Int J Numer Methods Biomed Eng 33(11):e2877
- Graner F, Glazier JA (1992) Simulation of biological cell sorting using a two-dimensional extended Potts model. Phys Rev Lett 69(13):2013. https://doi.org/10.1103/PhysRevLett.69.2013
- Ingber DE (2005) Mechanical control of tissue growth: function follows form. Proc Natl Acad Sci 102(33):11571. https://doi. org/10.1073/pnas.0505939102
- Lamouille S, Xu J, Derynck R (2014) Molecular mechanisms of epithelial-mesenchymal transition. Nat Rev Mol Cell Biol 15(3):178. https://doi.org/10.1038/nrm3758
- Lee J, Talman L, Peirce S, Holmes J (2019) Spatial scaling in multiscale models: methods for coupling agent-based and finite-element models of wound healing. Biomech Model Mechanobiol
- Lemmon CA, Romer LH (2010) A predictive model of cell traction forces based on cell geometry. Biophys J 99(9):L78. https://doi.org/10.1016/j.bpj.2010.09.024
- Li J, Barbone PE, Smith ML, Stamenović D (2018) Tensional homeostasis in multicellular clusters: effects of geometry and traction force dynamics. Tensional homeostasis in multicellular clusters: effects of geometry and traction force dynamics. bioRxiv p. 370437. https://doi.org/10.1101/370437
- Liu Z, Tan JL, Cohen DM, Yang MT, Sniadecki NJ, Ruiz SA, Nelson CM, Chen CS (2010) Mechanical tugging force regulates the size of cell-cell junctions. Proc Natl Acad Sci 107(22):9944. https://doi.org/10.1073/pnas.0914547107
- Maruthamuthu V, Sabass B, Schwarz US, Gardel ML (2011) Cell-ECM traction force modulates endogenous tension at cell-cell contacts. Proc Natl Acad Sci 108(12):4708. https://doi.org/10.1073/pnas.1011123108
- Mathur J, Sarker B, Pathak A (2018) Predicting collective migration of cell populations defined by varying repolarization dynamics. Biophys J 115(12):2474. https://doi.org/10.1016/j.bpj.2018.11.013
- Mendonsa A, Na TY, Gumbiner BM (2018) E-cadherin in Contact Inhibition and Cancer. Oncogene 37(35):4769. https://doi.org/10.1038/s41388-018-0304-2
- Mertz AF, Banerjee S, Che Y, German GK, Xu Y, Hyland C, Marchetti MC, Horsley V, Dufresne ER (2012) Scaling of traction forces with the size of cohesive cell colonies. Scaling of traction forces with the size of cohesive cell colonies. Phys Rev Lett 108(19):198101. https://doi.org/10.1103/PhysRevLett.108.198101
- Mohan A, Schlue KT, Kniffin AF, Mayer CR, Duke AA, Narayanan V, Arsenovic PT, Bathula K, Danielsson BE, Dumbali SP et al (2018) Spatial proliferation of epithelial cells is regulated by E-cadherin force. Biophys J 115(5):853
- Narayanan V, Schappell LE, Mayer CR, Duke AA, Armiger TJ, Arsenovic PT, Mohan A, Dahl KN, Gleghorn JP, Conway DE (2020)
  Osmotic gradients in epithelial acini increase mechanical tension across E-cadherin, drive morphogenesis, and maintain homeostasis. Curr Biol 30:1. https://doi.org/10.1016/j.cub.2019.12.025
- Nelson CM, Jean RP, Tan JL, Liu WF, Sniadecki NJ, Spector AA, Chen CS (2005) Emergent patterns of growth controlled by multicellular form and mechanics. Proc Natl Acad Sci 102(33):11594. https://doi.org/10.1073/pnas.0502575102
- Ng MR, Besser A, Brugge JS, Danuser G (2014) Mapping the dynamics of force transduction at cell–cell junctions of epithelial clusters. eLife 5(3):e03282. https://doi.org/10.7554/eLife.03282
- Oelz D, Khataee H, Czirok A, Neufeld Z (2019) Polarization wave at the onset of collective cell migration. Phys Rev E 100(3):032403
- Okuda S, Inoue Y, Adachi T (2015) Three-dimensional vertex model for simulating multicellular morphogenesis. Biophys Physicobiol 12:13
- Puliafito A, Hufnagel L, Neveu P, Streichan S, Sigal A, Fygenson DK, Shraiman BI (2012) Collective and single cell behavior in



- epithelial contact inhibition. Proc Natl Acad Sci 109(3):739. https://doi.org/10.1073/pnas.1007809109
- Ramis-Conde I, Drasdo D, Anderson AR, Chaplain MA (2008) Modeling the influence of the E-cadherin-β-catenin pathway in cancer cell invasion: a multiscale approach. Biophys J 95(1):155
- Ramis-Conde I, Chaplain MA, Anderson AR, Drasdo D (2009) Multiscale modelling of cancer cell intravasation: the role of cadherins in metastasis. Phys Biol 6(1):016008
- Rens EG, Merks RM (2019) Cell shape and durotaxis follow from mechanical cell-substrate reciprocity and focal adhesion dynamics: a unifying mathematical model. arXiv preprint arXiv:1906.08962
- Rens EG, Merks RM (2017) Cell contractility facilitates alignment of cells and tissues to static uniaxial stretch. Biophys J 112(4):755
- Richardson WJ, Holmes JW (2016) Emergence of collagen orientation heterogeneity in healing infarcts and an agent-based model. Biophys J 110(10):2266
- Scarpa E, Szabó A, Bibonne A, Theveneau E, Parsons M, Mayor R (2015) Cadherin switch during EMT in neural crest cells leads to contact inhibition of locomotion via repolarization of forces. Dev Cell 34(4):421. https://doi.org/10.1016/j.devcel.2015.06.012
- Schlüter DK, Ramis-Conde I, Chaplain MA (2015) Multi-scale modelling of the dynamics of cell colonies: insights into cell-adhesion forces and cancer invasion from in silico simulations. J R Soc Interface 12(103):20141080
- Scott LE, Weinberg SH, Lemmon CA (2019) Mechanochemical signaling of the extracellular matrix in epithelial-mesenchymal transition. Front Cell Dev Biol 7

- Szabó A, Merks RM (2013) Cellular potts modeling of tumor growth, tumor invasion, and tumor evolution. Front Oncol 3:87
- Tan JL, Liu W, Nelson CM, Raghavan S, Chen CS (2004) Simple approach to micropattern cells on common culture substrates by tuning substrate wettability. Tissue Eng 10(5–6):865
- Thiery JP, Sleeman JP (2006) Complex networks orchestrate epithelial-mesenchymal transitions. Nat Rev Mol Cell Biol 7(2):131. https://doi.org/10.1038/nrm1835
- Trepat X, Wasserman MR, Angelini TE, Millet E, Weitz DA, Butler JP, Fredberg JJ (2009) Physical forces during collective cell migration. Nat Phys 5(6):426. https://doi.org/10.1038/nphys1269
- van Oers RFM, Rens EG, LaValley DJ, Reinhart-King CA, Merks RMH (2014) Mechanical cell–matrix feedback explains pairwise and collective endothelial cell behavior in vitro. Mechanical cell–matrix feedback explains pairwise and collective endothelial cell behavior in vitro. PLOS Comput Biol 10(8):e1003774. https://doi.org/10.1371/journal.pcbi.1003774
- Weinberg SH, Mair DB, Lemmon CA (2017) Mechanotransduction dynamics at the cell–matrix interface. Biophys J 112(9):1962

**Publisher's Note** Springer Nature remains neutral with regard to jurisdictional claims in published maps and institutional affiliations.

